Earth and Planetary Science Letters 534 (2020) 116074

Contents lists available at ScienceDirect

Earth and Planetary Science Letters

www.elsevier.com/locate/epsl

Enhanced continental weathering and large igneous province induced climate warming at the Permo-Carboniferous transition

Jianghai Yang [a,*], Peter A. Cawood [b], Isabel P. Montañez [c], Daniel J. Condon [d], Yuansheng Du [a], Jia-Xin Yan [a], Shaoquan Yan [e], Dongxun Yuan [f]

[a] State Key Laboratory of Biogeology and Environmental Geology & School of Earth Sciences, China University of Geosciences, Wuhan, 430074, China
[b] School of Earth, Atmosphere & Environment, Monash University, Melbourne, VIC 3800, Australia
[c] Department of Earth and Planetary Sciences, University of California, Davis, California 95616, USA
[d] NERC Isotope Geosciences Laboratory, British Geological Survey, Keyworth NG12 5GG, UK
[e] No. 4 Institute of Geological & Mineral Resources Survey of Henan, Zhengzhou, 450016, China
[f] Nanjing Institute of Geology and Palaeontology, Chinese Academy of Sciences, Nanjing 210008, China

ARTICLE INFO

Article history:
Received 30 July 2019
Received in revised form 20 December 2019
Accepted 6 January 2020
Available online 21 January 2020
Editor: T.A. Mather

Keywords:
mudrock
source weathering trends
early Permian
climate warming
large igneous province

ABSTRACT

Tracking climate change and its relationships with chemical weathering and massive volcanic activity in deep-time greatly improves our understanding of the Earth's climate system. The Permo-Carboniferous period is a critical time interval with million year-scale glacial-deglacial cycles and massive basaltic volcanism, such as the Skagerrak-Centered (also named Skagerrak or Jutland) large igneous province. To explore the volcanism-climate interactions in this period, we obtained high precision CA-TIMS U-Pb zircon ages for three tuffaceous layers from a cored upper Pennsylvanian-lower Permian marginal marine succession in southern North China. These ages calibrate the Permo-Carboniferous biostratigraphy between ~301–296 Ma in North China. From this dated core succession, mudrock samples and their calculated weathering index values were screened to constrain the weathering trends for the source landscapes and demonstrate a rapid increase with a subsequent decrease in source chemical weathering intensity during the period of ~299 to 296.5 Ma. These trends coincide with the southern Gondwana glacial records, low latitude temperature changes, relative sea-level variations, and shifts in atmospheric pCO_2 that together document an earliest Permian climate warming-cooling perturbation with a temperature maximum at ~298 Ma. This climate warming in the Permo-Carboniferous icehouse correlates with the emplacement of the Skagerrak-Centered large igneous province, which likely released voluminous CO_2 that led to climate warming during the Permo-Carboniferous transition. The immediately following cooling could possibly result from the rapid post-eruptional weathering of the massive basaltic rocks of this province in tropical latitudes, which would have sequestered atmospheric CO_2 and promoted return to cooler icehouse conditions. This study supports the assertation that massive basaltic volcanism could first cause rapid climate warming and then may have an overall net cooling effect as previously suggested for the Deccan Traps and the Central Atlantic Magmatic Province.

1. Introduction

Massive basaltic volcanism and associated mafic intrusions during large igneous province (LIP) events can release voluminous greenhouse gases (e.g., CO_2) into the atmosphere and potentially cause significant climate warming (e.g., Ernst and Youbi, 2017; Schaller et al., 2012). LIP basaltic rocks can also experience rapid post-eruptive weathering and thus effectively consume atmospheric CO_2 (Dessert et al., 2001; Schaller et al., 2012), returning the climate to cooler conditions (Jones et al., 2016; Schaller et al., 2012). Meanwhile continental weathering trends have discernable responses to climate change, with high weathering intensity corresponding to warm and humid climate and low weathering intensity to colder or drier conditions (e.g., Nesbitt and Young, 1982; Yang et al., 2014). Therefore, weathering, climate and LIP volcanism are mechanically linked, leading to punctuated climate fluctuations through Earth history (Ernst and Youbi, 2017; Dessert et al., 2001; Schaller et al., 2012). The Permo-Carboniferous transition (~302–297 Ma) represents one such critical period. This time interval coincides with the main emplacement of the Skagerrak-Centered (also alternatively named as Skagerrak and Jutland, Ernst

* Corresponding author.
E-mail address: yangjh@cug.edu.cn (J. Yang).

https://doi.org/10.1016/j.epsl.2020.116074

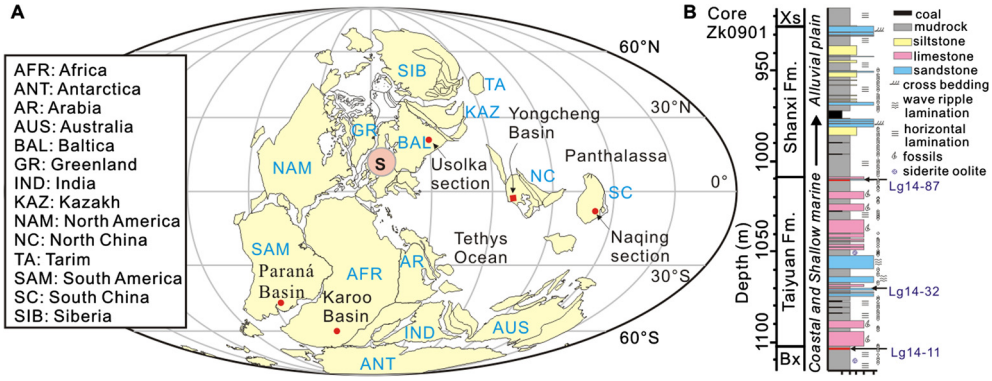

Fig. 1. Location and stratigraphic column for the studied Permo-Carboniferous strata of Benxi (BX), Taiyuan, Shanxi and Xiashihezi (XS) formations of core Zk0901 from southern North China. (A) ~300 Ma paleogeographic reconstruction modified after Torsvik et al. (2014) showing low-latitude position of North China block. Location of the Skagerrak-Centered LIP is marked by a pink circle. Also shown are the locations of Usolka section in Ural (Henderson et al., 2012), Naqing section in South China (Chen et al., 2016), Paraná Basin in South America (Griffis et al., 2018) and Karoo Basin in southern Africa (Scheffler et al., 2003). (B) Lithologic column with facies interpretation and stratigraphic positions of dated ash beds (arrows) and analyzed mudrock samples (spots). (For interpretation of the colours in the figure(s), the reader is referred to the web version of this article.)

and Youbi, 2017) LIP in NW Europe (Torsvik et al., 2008). It is associated with a notable climate warming in western tropical Pangaea (Tabor et al., 2013), the terminal deglaciation in the Paraná Basin of South America (Griffis et al., 2018), a Gondwana-wide transgression (Stollhofen et al., 2008; Griffis et al., 2019) and the enhanced interstadial weathering in southern Africa (Scheffler et al., 2003). The Permo-Carboniferous peak icehouse also initiated during this period (~298-297 Ma) and has been interpreted in terms of frequent explosive intermediate-felsic volcanism (Soreghan et al., 2019). However, a paucity of high-resolution climate proxy records and overall lack of high-precision dated chronostratigraphic correlation have hindered establishing potential basaltic LIP-climate-weathering linkages for this time period.

To test this possible causal relationship among the LIP event, climate change and chemical weathering, we here report high-precision zircon U-Pb ages for, and derive a record of, tropical weathering trends from a cored uppermost Carboniferous through the lower Permian succession in southern North China. Our data, combined with published and precisely age-constrained climate records, suggest a climate warming at the Permo-Carboniferous transition that likely corresponds with the emplacement of the Skagerrak-Centered LIP event.

2. Samples and analytical methods

North China occupied a low-latitude position surrounded by the Tethys Ocean to the west and the Panthalassic Ocean to the east during the Pennsylvanian through early Permian (Fig. 1A; Torsvik et al., 2014; Cawood et al., 2013). In North China, ubiquitous littoral-deltaic coal-bearing siliciclastic and carbonate rocks accumulated in association with an ever-wet flora during the late Pennsylvanian to early Permian (Wang, 1985; Tabor and Poulsen, 2008). Core Zk0901 was recovered from the Yongcheng Basin in southeastern North China (Fig. 1A). It is preserved in a dedicated core storage facility and is thus free of modern surface weathering. It was drilled through the late Pennsylvanian-Permian strata to the underlying Ordovician limestones. The sampled core succession of Benxi, Taiyuan, Shanxi, and lowest Xiashihezi formations consists of black-grey mudrocks generally with horizontal lamination, siltstones and wave ripple-laminated or cross-bedded fine- to medium-grained sandstones, along with several coal seams 0.05-2 m thick, and bio-clastic limestones (Fig. 1B). The Benxi and Taiyuan formations are broadly coastal and shallow marine deposits of very similar aspect to the cyclothemic successions of the North America and Europe (Wang, 1985; Schmitz and Davydov, 2012 and references therein). The succession becomes progressively shallower upsection with more alluvial plain and nonmarine environments in the Shanxi and Xiashihezi formations (Feng, 2012).

Three tuffaceous layers (~1-10 cm thick) were sampled for single-zircon CA-TIMS (chemical-ablation isotope-dilution thermal ionization mass spectrometry) U-Pb dating. Sample Lg14-11 is a tuffaceous claystone collected from the uppermost of Benxi Formation, sample Lg14-32 is a crystalline-lithic tuff collected from the middle part of Taiyuan Formation, and sample Lg14-87 is a tuffaceous sandstone collected from the uppermost of Taiyuan Formation (Fig. 1B). A total of 119 mudrock samples were collected from core Zk0901 through the Benxi Formation to the middle Shanxi Formation for mineralogical and geochemical analysis.

Zircon grains separated from the three ash samples were dated using CA-TIMS protocols at the NERC Isotope Geoscience Laboratory of the British Geological Survey, Nottingham, UK. Leached zircons were spiked with the mixed ^{202}Pb-^{205}Pb-^{233}U-^{235}U EARTHTIME tracer solutions (ET2535; Condon et al., 2015). Mineralogical analyses by X-ray diffraction were performed with a PANalytical X'Pert Pro model instrument at the State Key Laboratory of Geological Process and Mineral Resources (GPMR), China University of Geosciences (Wuhan). The analytical error is ~5%. Major element analyses were conducted on a PANalytical Axios X-ray florescence spectrometer at ALS Chemex (Guangzhou, China). Analytical accuracy is better than 5% and uncertainty less than 5% for all major elements. Trace element abundances were measured on an Agilent 7500a ICP-MS at the GPMR. Analytical precision and accuracy are generally better than 5% for most trace elements. Detailed analytical methods and data are available in the Supplementary files.

3. Results

3.1. High-precision CA-TIMS zircon U-Pb ages

Separated zircon grains were observed and imaged under transmitted light microscopy. Samples Lg14-11 and Lg14-32 yield zircon populations with elongate prismatic morphologies (generally >3:1 long-to-width ratio and >100 μm in their longest dimensions) and visible melt inclusions. The zircon population of sample Lg14-87, however, is more complex and includes sub-equant grains with slightly rounded to prismatic morphologies. By careful selection, only euhedral, clear grains devoid of optically recognizable cores were chosen for analysis. U-Pb ages are reported with 2σ errors (Table S1). Weighted mean age errors are herein reported as ± X/Y/Z Ma, representing analytical/analytical + tracer solution/analytical + tracer solution + ^{238}U decay constant uncertainties.

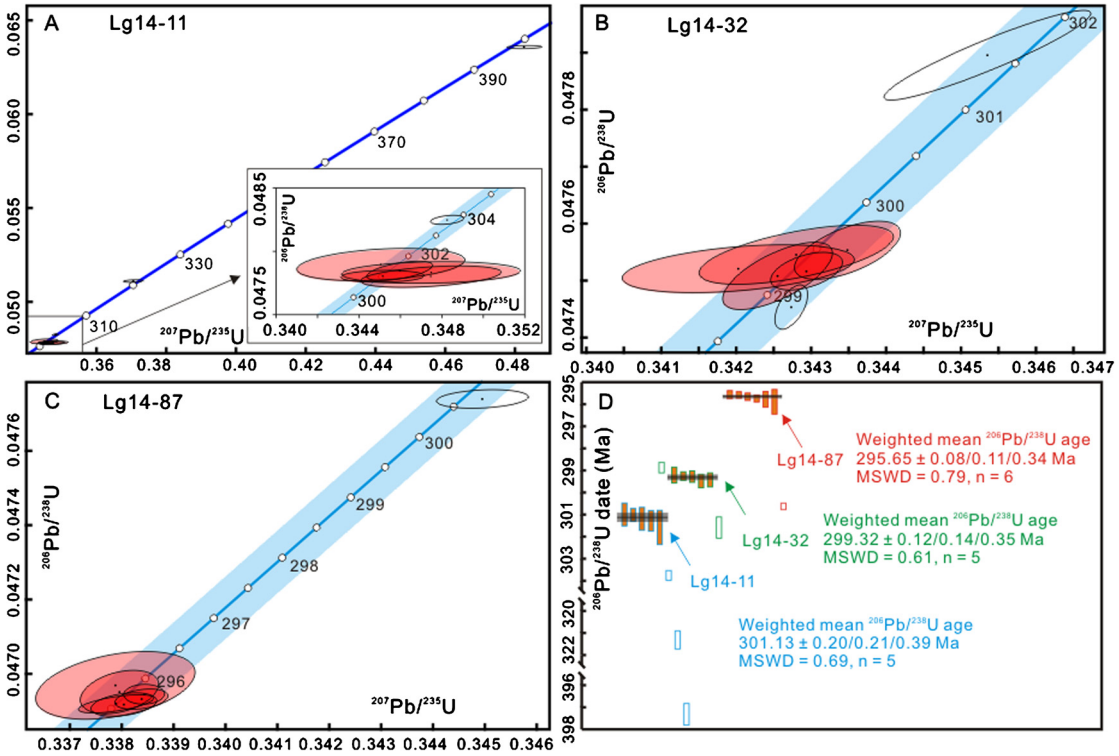

Fig. 2. Zircon U-Pb Concordia diagrams (A, B and C) and ranked $^{206}Pb/^{238}U$ age plot with weighted mean ages (D). Only the orange shaded analyses were incorporated for the calculation of the weighted mean age.

Eight single-zircon grains of sample Lg14-11 were analyzed and yielded concordant U-Pb data (Fig. 2A). Three analyses yield relatively older $^{206}Pb/^{238}U$ dates of 303.76–397.32 Ma and are probably of xenocrystic origin. The remaining five analyses form a significant cluster with a weighted mean $^{206}Pb/^{238}U$ age of 301.13 ± 0.20/0.21/0.39 Ma with an MSWD (mean squared weighted deviation) value of 0.69 (Fig. 2D). Seven single-zircon grains were analyzed from Lg14-32 and yielded concordant U-Pb data (Fig. 2B). One grain has obvious inheritance yielding an age of 301.59 ± 0.4 Ma. Another analysis is slightly younger at 298.87 ± 0.24 Ma and suggests incomplete mitigation of Pb loss despite the chemical abrasion approach. The five remaining analyses form a significant cluster with a weighted mean $^{206}Pb/^{238}U$ age of 299.32 ± 0.12/0.14/0.35 Ma with an MSWD value of 0.59 (Fig. 2D). Seven zircon grains from Lg14-87 were analyzed individually and yielded concordant U-Pb data (Fig. 2C). One analysis is an obvious outlier with dispersion beyond that expected due to analytical scatter and a $^{206}Pb/^{238}U$ age of 300.65 ± 0.15 Ma, older than the main population. Excepting this xenocrystic grain, the other 6 analyses yield a weighted mean $^{206}Pb/^{238}U$ age of 295.65 ± 0.08/0.11/0.34 Ma with an MSWD value of 0.82 (Fig. 2D). The reported MSWD value for each weighted mean lies within its 95% confidence interval, indicating no excess geological scatter in the data. We herein interpret the three weighted mean ages as the eruption ages of the ashes, thus indicating the time of accumulation of the enclosing sedimentary layers.

3.2. Mudrock mineral and geochemical compositions

Major constituents of the mudrock samples are clay minerals, quartz and feldspars with generally low concentrations (each less than 5%) of calcite, ankerite, siderite and pyrite (Table S2). High carbonate mineral contents were detected in three samples (C14-16, C14-64 and C14-65) along with high percentages of CaO, MgO and Fe_2O_{3T} (Table S3). Mudrocks have a large range of K_2O (0.12–6.87%) with varied K_2O/Al_2O_3 (Table S4) and K_2O/Na_2O ratios (<0.01–0.23 and 0.92–52.77, respectively). Over the entire sampled succession, analyzed mudrocks show a generally narrow range of clay minerals/quartz ratio (3.5–5.5) and Al/Si molar ratio (Al/Si*, 0.3–0.5). In contrast, mudrocks from the Benxi Formation and the lower Taiyuan Formation display much larger variations in these two ratios (3.3–31.3 and 0.1–1.1, respectively; Table S4). The Zr/Sc ratio varies in the range of ~10-30 for most samples but can be high (>30) for some samples. The Th/Sc ratio has a positive correlation with Zr/Sc ratio (r^2 = 0.52) and changes from 0.5 to 3.0 with most samples in the range of 0.7-1.3. The La/Yb ratio varies from 1.7 to 35.3 with most samples in the range of 12-20 with an average of 16.5. The Zr/Ti ratio also has a limited variation in the range of ~0.03–0.08 (Table S4) for all but ten mudrocks (>0.09). The samples with higher Zr/Ti ratio possess correspondingly lower Na/Zr ratios.

3.3. Mudrock weathering index values

We here combine mineral index of alteration (MIA, Johnsson, 1993), weathering index of Parker (WIP, Parker, 1970), chemical index of alteration (CIA, Nesbitt and Young, 1982), chemical index of alteration without CaO (CIX, Dinis et al., 2017), sodium weathering index (α^{Al}_{Na}, Garzanti et al., 2013) and sodium depletion index (τ_{Na}, Rasmussen et al., 2011) to quantify the chemical weathering intensity experienced by the sources to the mudrocks. Values of these weathering indices are calculated according to the formulae outlined in Table S5. Previous studies have shown that the dominant source for the early Permian sedimentary rocks in the Yongcheng Basin (Yang et al., 2014; 2016) corresponds with the composition of the upper continental crust of the southern North China craton (Gao et al., 1998). This inference is reasonable because in this study most analyses plot along the predicted weathering trend (Nesbitt and Young, 1984) of the southern North China upper continental crust in the AL_2O_3-CaO^*+Na_2O-K_2O (A-CN-K) diagram (Fig. 3A; Fedo et al., 1995). Furthermore, these samples have Zr/Ti, Th/Sc and La/Yb ratios, used as provenance indicators (e.g.,

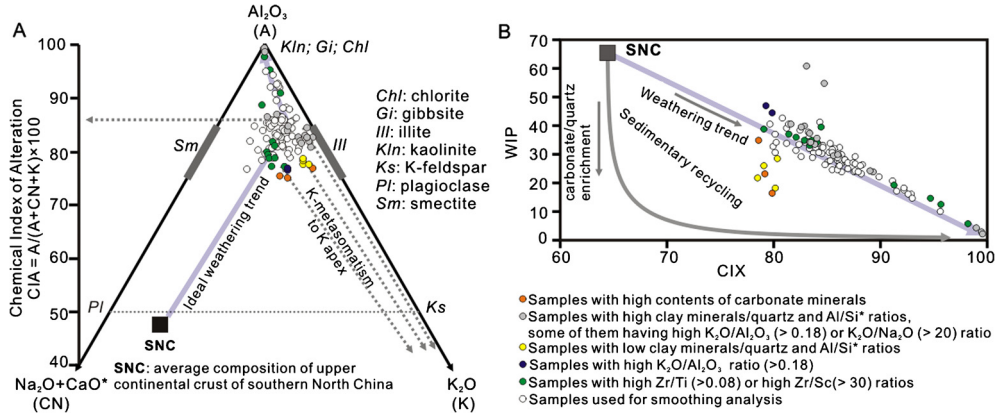

Fig. 3. A-CN-K (Al_2O_3-Na_2O+CaO*-K_2O) diagram with CIA scale on the left (A, Fedo et al., 1995) and CIX-WIP plot (B, Dinis et al., 2017) for the analyzed Zk0901 mudrock samples. In A-CN-K diagram, mudrock samples plot in the intermediate-intense weathering zones and generally mimic the ideal weathering trend of the southern North China upper continental crust (SNC, Gao et al., 1998). In CIX-WIP plot (Dinis et al., 2017), mudrock samples mainly define a linear relationship tracking the weathering trend of the southern North China upper continental crust and suggest a first-cycle derivation from the source region in southern North China. There are some samples plotting off obviously the source weathering trend lines in A-CN-K and CIX-WIP diagrams. These samples show high Mg-Ca carbonate mineral contents or have low clay mineral/quartz and Al/Si* ratios, or present high K_2O/Al_2O_3 or K_2O/Na_2O ratios.

Scheffler et al., 2003), close to that of the southern North China upper continental crust (Table S4; Gao et al., 1998). Therefore, the composition of the southern North China upper continental crust is used as the average source rock to calculate α^{Al}_{Na} and τ_{Na} values for the analyzed mudrock samples. Obtained values of MIA, WIP, CIA, CIX, α^{Al}_{Na} and τ_{Na} range from 0.60 to 1.0, from 2.0 to 60.8, from 75.1 to 99.3, from 78.4 to 99.5, from 2.6 to 210.4 and from −0.99 to −0.55, respectively (Table S4).

4. An age model for the Permo-Carboniferous succession in North China and correlation with the Euramerican successions

The age of the Permo-Carboniferous strata in North China is only broadly constrained based on biostratigraphy and has large uncertainties (Wang and Qi, 2003; Shen et al., 2019). The Permo-Carboniferous boundary has been placed at the bottom, in the middle, or at the top of the Taiyuan Formation in southern North China (Pei, 2004; Wang and Qi, 2003 and references therein). Our dated tuffaceous layers bracket the strata of the Taiyuan Formation except for the top limestones (Fig. 1B). These high-precision ages indicate a well-constrained late Gzhelian (Late Pennsylvanian) to late Asselian (early Cisuralian) age for this formation (Fig. 4), according to the latest timescale for the Permian (Shen et al., 2019). The obtained age of 299.32 Ma from the middle Taiyuan Formation is close to the Permo-Carboniferous boundary age of 298.9 ± 0.15 Ma (Schmitz and Davydov, 2012) and thus constrains the Permo-Carboniferous boundary to the middle part of the Taiyuan Formation in the Yongcheng Basin. Limestones from the top of the formation in a section close to this basin yield a *Sweetognathus* conodont fauna suggesting a middle Sakmarian to early Artinskian age (Gao et al., 2005). This biostratigraphic age would suggest an unconformity between the dated tuffaceous sandstone with age of ~ 295.65 Ma and the top limestones in the Taiyuan Formation if the latter also have the same conodont fauna. However, there is no corresponding geological evidence observed for an unconformity in the sampled core succession. Importantly, this reported fauna is also proposed to contain *Adetognathus* (= ?*Sweetognathus sulcatus* in Gao et al., 2005), which became extinct in the lowest conodont biozone (*Sweetognathus binodosus*) of the Sakmarian (Fig. 4; Henderson, 2018; Shen et al., 2019). If so, this fauna can be recalibrated to a latest Asselian age, which is consistent with our high-precision dating results. Unfortunately, we do not have the conodont elements reported in Gao et al. (2005) to confirm this inference. Detailed conodont biostratigraphic work needs to be undertaken on this strata interval.

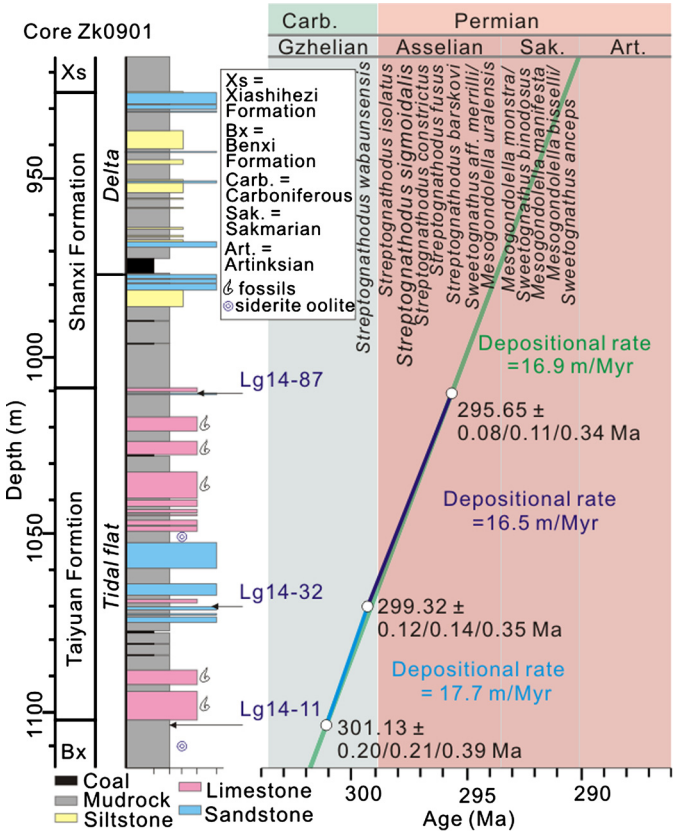

Fig. 4. Devised age model through the core Zk0901 succession based on time scale and conodont zonation of Shen et al. (2019) and Henderson (2018). Abbreviations: Sak-Sakmarian, Art-Artinskian, Bx-Benxi Formation, Xs-Xiashihe Formation.

Based on the three high-precision zircon U-Pb ages, three average depositional rates of 17.7 ± 2.2 m/Myr, 16.5 ± 0.6 m/Myr, and 16.9 ± 0.7 m/Myr, without compaction correction, can be calculated for the strata intervals between sample Lg14-11 and Lg14-32, between Lg14-32 and Lg14-87, and between Lg14-11 and Lg14-87, respectively. Given this concordance in depositional rate, we assume an overall average sediment accumulation rate of 16.9 m/Myr for the sampled strata interval and define an age model by linear interpolation (Fig. 4). This age model tightly constrains the studied succession of the Benxi, Taiyuan and Shanxi for-

mations to within the late Gzhelian-Sakmarian (Fig. 4; Henderson, 2018; Shen et al., 2019). Noting that the depositional rate could be variable in view of the shift in lithology and sedimentary facies especially for the interval above Sample14-87, the proposed linear age model may have large uncertainties. In spite of this deficiency, a model age of ~291 Ma is acquired for the top Shanxi Formation (Fig. 4) in agreement with a tuff zircon U-Pb age of 293.0 ± 2.5 Ma reported from the upper Shanxi Formation in the same basin (Yang et al., 2014), although the latter age has a large uncertainty and cannot provide a precise age constraint on the strata.

In North China, the Taiyuan Formation consists of cyclic deposits of coals, shales, sandstones and limestones (Yang et al., 2017; Wang, 1985) and has been tentatively linked to glacial eustatic transgressive-regressive episodes (Yang et al., 2017). In the Euramerican segment of tropical Pangea, the Permo-Carboniferous stratigraphic cyclothems have long been recognized as a far-field effect of Gondwana glaciation and associated global climate changes (Eros et al., 2012; Schmitz and Davydov, 2012 and references therein). High-precision radiometric dating and high-resolution conodont biostratigraphic work has enabled Pan-Euramerican correlations of these late Paleozoic cyclothemic successions in disparate basins (Eros et al., 2012; Schmitz and Davydov, 2012 and references therein). The North China succession has been noted to mimic the Pennsylvanian-early Permian cyclothems of Euramerica (Yang et al., 2017). Our high-precision zircon U-Pb ages provide a tight age constraint for the Taiyuan Formation in southern North China and enable precise correlation with the radiometrically dated, conodont biostratigraphically constrained, latest Pennsylvanian to earliest Permian successions in Euramerica (Schmitz and Davydov, 2012 and references therein).

5. Permo-Carboniferous weathering trends in the southern North China

Muds/mudrocks have the potential to provide valuable information on the weathering intensity of their source landscapes (e.g., Nesbitt and Young, 1982; Garzanti et al., 2013; Scheffler et al., 2003). For the studied mudrocks, calculated MIA, CIA, CIX, WIP, α^{Al}_{Na} and τ_{Na} values are plotted along the age model to track their source weathering trends (Fig. 5). Of the 119 analysed mudrocks, the majority preserve compositional variations predominantly related to chemical weathering of the source, but 38 samples show mineral and geochemical characteristics indicating effects of diagenetic alteration, hydrodynamic sorting and recycling, or provenance change (Figs. 3 and 5; Fedo et al., 1995; Garzanti et al., 2013; Garzanti and Resentini, 2016; Lupker et al., 2013; von Eynatten et al., 2016). The criteria by which they were excluded are outlined in the supplementary data files.

The remaining 81 mudrock samples have low K_2O/Al_2O_3 ratios and show a narrow variation in clay minerals/quartz, Al/Si* and Zr/Ti ratios, with the latter close to that of the southern North China upper continental crust (Fig. 5). They have CIA values, the most widely used weathering index, that display a positive correlation with MIA ($r^2 = 0.45$, $P < 0.001$), CIX ($r^2 = 0.90$, $P < 0.001$) and α^{Al}_{Na} ($r^2 = 0.72$, $P < 0.001$), and a negative correlation with WIP ($r^2 = 0.71$, $P < 0.001$) and τ_{Na} ($r^2 = 0.42$, $P < 0.001$). On the other hand, CIA values are poorly correlated with clay minerals/quartz, Zr/Sc, Zr/Ti and Th/Sc ratios ($r^2 = 0.02$, 0.03, 0.03 and 0.01, respectively), which are indicators of dynamic sorting, sedimentary recycling and provenance change (Johnsson, 1993; von Eynatten et al., 2016; Garzanti and Resentini, 2016 and references therein). The results also show poor correlation of Al/Si* ratio with clay minerals/quartz ($r^2 = 0.06$, $P < 0.001$) and Zr/Zn ratios ($r^2 = 0.09$, $P < 0.001$), all of which were used to monitor grain-size variation for silt-clay sediment (Lupker et al., 2013; von Eynatten et al., 2016). These relationships suggest that the sample compositional trends are unlikely controlled by grain size change and thus have little or no sorting effects. In addition, these samples dominantly plot along the ideal weathering trend of the southern North China upper continental crust on the A-CN-K (Fig. 3A) and the CIX-WIP (Fig. 3B) diagrams. This indicates a persistent sediment supply from a source in southern North China (Fedo et al., 1995; Yang et al., 2016) and implies little or no effect on the sample compositional trends from sedimentary recycling (Dinis et al., 2017; Garzanti et al., 2013). An insignificant influence from sedimentary recycling is further supported by the notable stratigraphic framework in North China with Permo-Carboniferous sequences disconformably overlying lower Paleozoic carbonates (Wang, 1985), which cannot provide a recycled siliciclastic source (Johnsson, 1993). Therefore, these screened mudrock samples retain source chemical weathering signals, and their sequential variations of calculated MIA, CIA, CIX, WIP, α^{Al}_{Na} and τ_{Na} values should accordingly reflect the chemical weathering trends in the source (e.g., Johnsson, 1993; Nesbitt and Young, 1982; Scheffler et al., 2003). These variations in chemical weathering trends (Fig. 5) reveal a remarkable increase, followed by an immediate decrease of similar magnitude in weathering intensity, in the uppermost Carboniferous to lower Asselian interval (~299-296.5 Ma) with relatively smaller fluctuations in the rest of the Asselian interval. The lowest Asselian mudrocks have much higher CIA values than those in the rest of the studied interval with the former and latter comparable to that of the river mouth muds in the humid equatorial and subequatorial Africa, respectively (Fig. 5; Dinis et al., 2017; Garzanti et al., 2013).

6. Implication for an earliest Asselian climate warming

A record of source weathering trends for the end-Carboniferous to early Permian (~300-290 Ma) for southern North China emerges when the results of this study are integrated with previously published mudrock data from the upper Shanxi Formation and bottom of the Xiashihezi Formation in core Zk090 (Yang et al., 2016). The observed variation in CIA values from Zk0901 is comparable to that recorded in time-equivalent deposits of the upper Dwyka to bottom Ecca Group in South Africa (Fig. 6A; Scheffler et al., 2003; Stollhofen et al., 2008). In addition to a significant Sakmarian increase in CIA values (Yang et al., 2014), corresponding to the early Permian glacial to postglacial transition (Scheffler et al., 2006), both the CIA trends from equational North China and high-latitude South Africa display an increase at the Permo-Carboniferous boundary (~299 Ma) and present high values in the earliest Asselian (Fig. 6A). Corresponding to this earliest Asselian high weathering intensity period is the interstadial phase of the Hardap Shale Member at the top of the deglaciation sequence III of the Dwyka Group (Fig. 6A). The top of Hardap Shale member has been tightly constrained at ~296.5 Ma by CA-TIMIS method (Griffis et al., 2019). Biostratigraphically, this shale member of Dwyka Group can be correlated with the postglacial sedimentary rocks of the uppermost Itararé Group in Paraná Basin (Taboada et al., 2016), where the onset of deglaciation has been well dated at around the Permo-Carboniferous boundary (>298 Ma, Griffis et al., 2018). Latest Gzhelian-earliest Asselian deglacial climate warming has also been documented in Eastern Gondwana and NE Russia near the paleo-pole by shallow marine fossil data (Davydov et al., 2013; Davydov and Biakov, 2015). This correlation supports the linkage of high weathering intensity with deglacial warming and argues for a global climate control on the weathering trends.

We here apply a statistically tested hypothesis that weathering is approximately supply-limited in most hillslope landscapes (e.g., Ferrier et al., 2016) to the eroding Permo-Carboniferous landscapes in southern North China. Modern surface soils in a supply-limited weathering regime tend to be chemically depleted to an

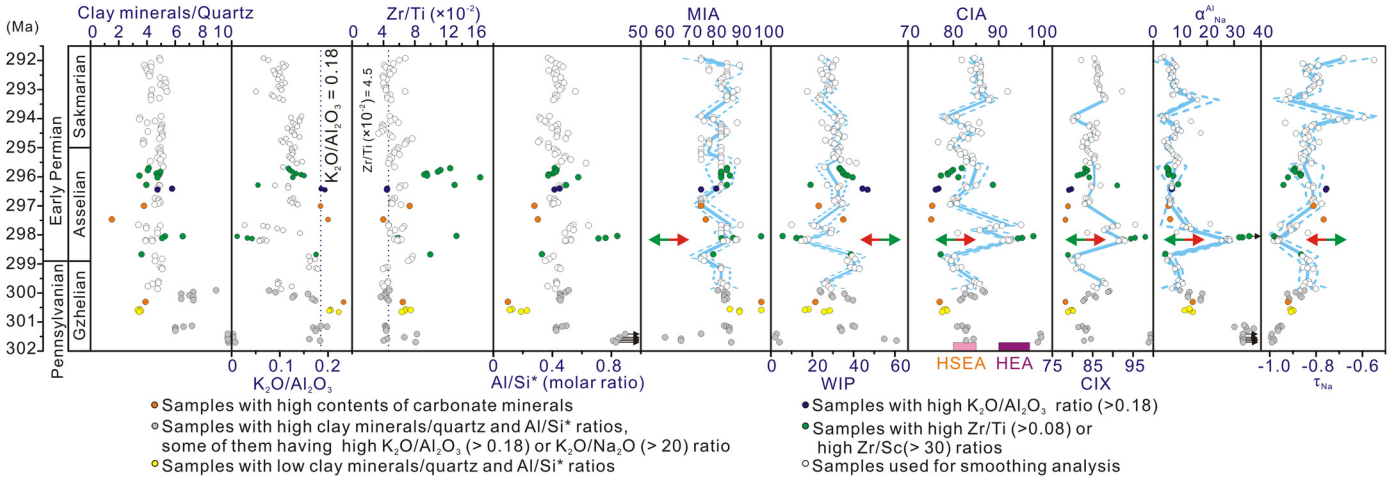

Fig. 5. Stratigraphic variations of mineralogical and geochemical proxies for the analyzed Zk0901mudrock samples. Locally estimated scatterplot smoothing trendlines using PAST software (http://folk.uio.no/ohammer/past/, 0.1 smoothing, solid lines) with 2.5% and 97.5% bootstrapped errors (dashed lines) are shown for MIA, WIP, CIA, CIX, α^{Al}_{Na} and τ_{Na} values (see the Data Repository for details). In the weathering index panels, red and green arrows indicate more and less weathered directions, respectively. The CIA value ranges for river mouth muds in humid subequatorial and equatorial Africa (HSEA and HEA, Dinis et al., 2017; Garzanti et al., 2013) are also shown for comparison. The K_2O/Al_2O_3 and Zr/Ti ratios of the southern North China upper continental crust are indicated (vertical blue dotted lines). Only the samples used for smoothing analysis are plotted in Fig. 6.

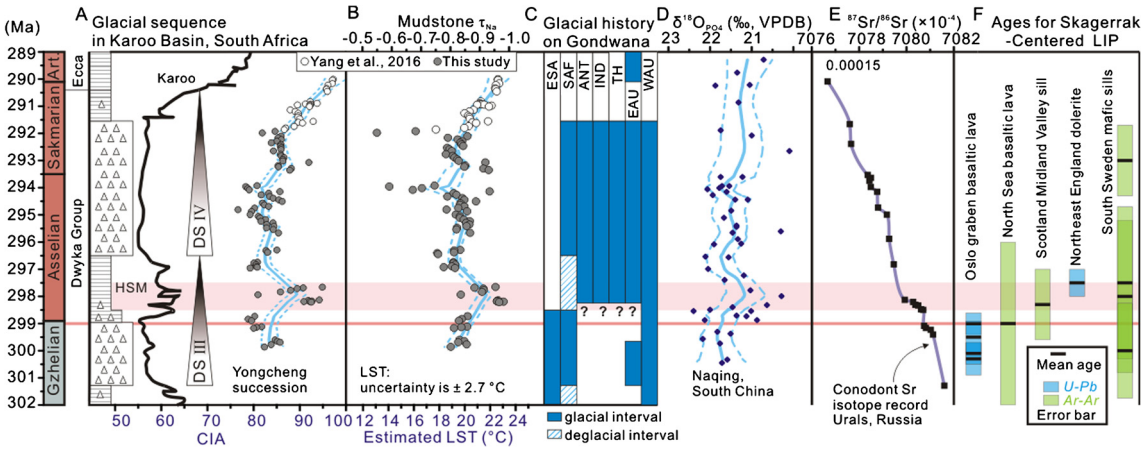

Fig. 6. Global correlations of climate and weathering records across the Permo-Carboniferous transition. (A) Karoo succession spanning the glacial Dwyka Group to the base of post-glacial Ecca Group in South Africa constrained by zircon U-Pb ages (Stollhofen et al., 2008; Griffis et al., 2019) and its CIA trend (Scheffler et al., 2003) compared to that of Yongcheng succession (Zk0901). HSM: the Hardap Shale Member (HSM) at the top of the deglacial sequence III (DS III) of the Dwyka Group. HSM can constrained by CA-TISM zircon U-Pb dating and biostratigraphic correlation in the age range of ~299-296.5 Ma (Griffis et al., 2019; Stollhofen et al., 2008; Taboada et al., 2016). (B) Temporal distribution of τ_{Na} for Zk0901 with corresponding LST (bottom axis) estimated using the transfer function of Yang et al. (2016). (C) Latest Carboniferous-early Permian glaciation history for paleo-Gondwanan regions of eastern South America (ESA), South Africa (SAF), Antarctica (ANT), India (IND), Tethys Himalaya (TH), western Australia (WAU) and east Australia (EAU). (D) Sequential variation of conodont $\delta^{18}O$ from Naqing section of South China (Chen et al., 2016). (E) High-precision dating calibrated stratigraphical variation of conodont $^{87}Sr/^{86}Sr$ ratio from Urals (Henderson et al., 2012). (F) U-Pb and Ar-Ar dating results for the Oslo graben basaltic lava, North Sea basalts, West Midland Valley alkaline sill, northeastern England dolerite and south Sweden mafic sills of the Skagerrak-Centered LIP (Corfu and Dahlgren, 2008; Hamilton and Pearson, 2011; Heeremans et al., 2004; Monaghan and Pringle, 2004; Torsvik et al., 2008 and references therein; Table S6). Blue solid and dashed lines in B, C and D are the locally estimated scatterplot smoothing trendlines (PAST, 0.2 smoothing) and bootstrapped errors (2.5% and 97.5%), respectively. Pink shading indicates the interval (~298.5-297.5 Ma) with the earliest Asselian temperature peak and the red line denotes the onset of the climate warming in the latest Gzhelian (~299 Ma).

extent (weathering intensity) largely controlled by precipitation and temperature (Ferrier et al., 2016 and references therein; Riebe et al., 2004). Because there was an ever-wet coal-forming climate in North China during the early Permian (Montañez and Poulsen, 2013; Tabor and Poulsen, 2008), the observed weathering trends might not be controlled by water availability, but likely indicate changes in land surface temperature (Yang et al., 2016). Using the τ_{Na}–based transfer function (Yang et al., 2016), a reconstructed land surface temperature trend through the sampled succession suggests a distinct warming of ~3-5 °C (with an uncertainty of 2.7 °C), immediately followed by a rapid cooling in the early Asselian and generally lower temperatures in the middle Asselian-early Sakmarian (Fig. 6B).

This earliest Asselian warming may have already initiated in the latest Gzhelian (~300-299 Ma, Fig. 6B). It is correlated with a Gondwana-wide deglacial transgression (Stollhofen et al., 2008 and references therein) and thus reflects a significant retreat of the Gondwana ice sheet (Fig. 6). The subsequent cooling is temporally correlated with the resumed tillite deposition in South Africa (Fig. 6C), marking an ice sheet expansion event in Gondwana. It is important to note that there are near-field glacial facies in other parts of Gondwana (India, Tethys Himalaya, Australia and Antarctica) (Fig. 6C, Montañez and Poulsen, 2013; Torsvik et al., 2014; Isbell et al., 2012; Fielding et al., 2008), representing a deep-freeze climate state for much of the Asselian. Though not well age constrained, stratigraphic correlations may also suggest deglacial de-

posits in Himalayas and western Australia in eastern Gondwana at around the Permo-Carboniferous transition in addition to the South America (Davydov et al., 2013; Garzanti et al., 1998; Griffis et al., 2019; Taboada et al., 2016). Coincidently, conodont $\delta^{18}O$ values from South China show a ~1‰ decrease and a subsequent increase in the earliest Asselian (Fig. 6D; Chen et al., 2016), denoting a consistent pattern for the tropical sea water temperature change. During this earliest Asselian warm interval there is a short-term sea level high (~297.5 Ma, Haq and Schutter, 2008). Consequently, a coincidence of deglaciation, higher temperature and sea-level high stand likely defined a climate warm interval in the first ~2 m.y. in the Asselian immediately predating the late Paleozoic maximum icehouse.

7. Causal link with the Skagerrak-Centered LIP?

The earliest Asselian temperature maximum is apparently comparable to that in the middle Miocene (~17-15 Ma), which was associated with ice sheet retreat and climate warming during the late Cenozoic icehouse and has been causally linked to the eruptive CO_2 release of the Columbia River Flood Basalts (McKay et al., 2014; Kasbohm and Schoene, 2018 and reference therein). Similarly, the hypothesized earliest Asselian climate warming is temporally overlapping with the massive basaltic eruptions and mafic intrusions of the Skagerrak-Centered LIP (Torsvik et al., 2008). Overall, this LIP magmatism may extend from the Late Carboniferous to early Permian (Torsvik et al., 2008). However, the main phase of basaltic volcanism in the Oslo graben and North Sea, and of mafic sills in Scotland, England and south Sweden, is constrained through U-Pb and Ar-Ar geochronology within a brief interval of ~300–298 Ma (Table S6; Corfu and Dahlgren, 2008; Heeremans et al., 2004; Monaghan and Pringle, 2004; Hamilton and Pearson, 2011; Timmerman et al., 2009). Although the uncertainties on these compiled ages for the Skagerrak-Centered LIP are large and need to be improved in the future, especially the Ar-Ar data, they are consistent with the hypothesis that the main basaltic phases of this LIP are temporally correlated with the earliest Asselian warming. As generally assumed and modelled for other LIPs (Dessert et al., 2001; Ernst and Youbi, 2017; Schaller et al., 2012), the Skagerrak-Centered LIP event may have resulted in a rapid release of voluminous CO_2 into the atmosphere, leading to a rise in atmospheric pCO_2. It is, however, difficult to quantify the amount of CO_2 emitted without knowing critical information like original volume, eruptive rate, and magmatic process of the LIP (Corfu and Dahlgren, 2008; Neumann et al., 2004; Self et al., 2006). Nonetheless, using a conservative volume estimate of ~1.5×10^5 km^3 for the erupted basalts in Skagerrak-Centered LIP (Neumann et al., 2004; Torsvik et al., 2008) and scaling based on data estimated for the Deccan basalts (Self et al., 2006), suggests a possible magmatic release of 1.4×10^3 Pg CO_2. Additional CO_2 emissions could come from contact metamorphism related to the voluminous intrusions of sills and dyke swarms in the LIP (McKay et al., 2014; Torsvik et al., 2008; Phillips et al., 2018). Importantly, the background atmospheric pCO_2 at the Permo-Carboniferous transition is quite low (Montañez et al., 2016) and would be sensitive to the change in the rate of magmatic CO_2 input. Therefore, the potential release of CO_2 during the emplacement of the Skagerrak-Centered LIP could potentially have resulted in a greenhouse warming in the earliest Permian (~299-298 Ma).

A subsequent rapid cooling (~298-296.5 Ma) after the earliest Asselian warming is indicated by the weathering trends in North China and the conodont $\delta^{18}O$ data from South China (Fig. 6). This cooling event is associated with a rapid drawdown of atmospheric pCO_2 (Montañez et al., 2016) and a lowering in short-term sea level (Haq and Schutter, 2008), although there are no high-precision age constraints for the latter two events. It might correspond with the onset of the early Permian peak icehouse (Soreghan et al., 2019). Based on global radio-isotopically dated intermediate-felsic eruption data, Soreghan et al. (2019) proposed a radiative forcing effect of explosive volcanic sulfate aerosols on the early Permian glacial acme. This climatic cooling effect is likely to provide an important control factor to the late Paleozoic ice age. However, the compiled explosive volcanic records in Soreghan et al. (2019) have a temporal resolution of 10 Myr, because of their general large uncertainties in determined ages, which is hard to reconcile with our high-resolution (<1 Myr) climate variations in the Permo-Carboniferous transition. Therefore, another climate cooling mechanism is hinted for the early Asselian cooling.

This cooling trend immediately following a rapid warming is reminiscent of the negative climate feedback of LIP basaltic weathering as proposed for the Deccan Traps (Dessert et al., 2001) and Central Atlantic Magmatic Province (Schaller et al., 2012). In the earliest Asselian there is a remarkable decreasing trend of marine $^{87}Sr/^{86}Sr$ based on high-precision zircon U-Pb dating of the calibrated conodont strontium isotopic curve from the Ural successions (Fig. 6E, Henderson et al., 2012). This has a rate of ~0.00015/Myr (Henderson et al., 2012), much higher than that for the whole Early Permian (Korte and Ullmann, 2018). The overall decrease in the Early Permian marine $^{87}Sr/^{86}Sr$ has been related to enhanced igneous activity or a reduction in radiogenic riverine Sr flux (Korte and Ullmann, 2018 and references therein). But these explanations are inconsistent with coincident low atmospheric pCO_2 and high pO_2 during the earliest Permian (Chen et al., 2018). This faster decreasing trend of marine $^{87}Sr/^{86}Sr$ during ~298.5 to 298 Ma is temporally correlated with the earliest Permian temperature maximum (Fig. 6E; Henderson et al., 2012). Considering its occurrence immediately following the emplacement of the Skagerrak-Centered LIP basalts, it is possible that the rapid chemical weathering of the basalt and the resultant influx of unradiogenic Sr into the ocean would partially account for the earliest Permian decrease in marine $^{87}Sr/^{86}Sr$. This linkage is supported by further evidence: (1) the volcanic rocks in Skagerrak-Centered LIP generally have low $^{87}Sr/^{86}Sr$ ratios in the range of ~0.703-0.705 (Neumann et al., 2004), (2) the Skagerrak-Centered LIP was emplaced in a humid tropical latitude (~11° N, Torsvik et al., 2014), and (3) the stratigraphic framework in this LIP suggests that the basaltic volcanic sequences have experienced extensive post-eruptional weathering and erosion at least in the early Permian (Neumann et al., 2004). In addition, LIP volcanic rocks are more chemically reactive to weathering than continental silicates and their chemical weathering tends to effectively consume atmospheric CO_2 (Dessert et al., 2001; Schaller et al., 2012). Importantly, models suggested that the LIP basaltic weathering could reduce the pCO_2 to below pre-eruptive levels and result in a cooler climate in 1-2 Myr (Dessert et al., 2001; Schaller et al., 2012). Following the assumptions for other LIPs (Ernst and Youbi, 2017 and references therein), the basaltic weathering of Skagerrak-Centered LIP could have likely driven the indicated atmospheric CO_2 drawdown and induced the subsequent climate cooling and widespread glaciation through the remaining Asselian and early Sakmarian stages of the early Permian.

8. Conclusions

Volcanism-climate interaction is an intriguing topic especially for the Permo-Carboniferous ice age with multiple glacial-deglacial cycles and massive pulses of felsic-basaltic volcanism. A cored Permo-Carboniferous succession in southern North China was studied in terms of geochronology and weathering geochemistry. Three tuff layers were dated with high-precision CA-TIMS single zircon U-Pb dating method and yield ages of 301.13 ± 0.20/0.21/0.39 Ma, 299.32 ± 0.12/0.14/0.35 Ma and 295.65 ± 0.08

/0.11/0.34 Ma. Assuming a consistent rate of sediment accumulation, a linear age model is proposed for, and contains, the sampled strata in age range between ~302-290 Ma. Systematic variations in calculated weathering index values from screened mudrock samples from this dated Permo-Carboniferous succession track weathering trends in the source landscapes in southern North China and indirectly indicate significant perturbations to climate. When integrated with geochronological and biostratigraphic data, the U-Pb calibrated climate proxy records from conodont fossils in South China and glacial deposits in Gondwana, the weathering trends for the North China succession developed in this study document an earliest Permian temperature maximum in the early Permian icehouse. Our new data compiled with literature studies support a causal linkage between this climate warming-cooling perturbation and the Skagerrak-Centered LIP through magmatic-metamorphic CO_2 emission and subsequent post-eruptional basaltic weathering and CO_2 drawdown, although further work on improving age constraints for this LIP event is to be encouraged.

Declaration of competing interest

The authors declare that they have no known competing financial interests or personal relationships that could have appeared to influence the work reported in this paper.

Acknowledgements

The authors thank J. Chen for discussions and E. Garzanti and R. Ernst for comments on the early version of the manuscript. Chris Fielding, an anonymous reviewer and Editor Tamsin Mather are gratefully acknowledged for their constructive reviews and guidance. This study was financially supported by National Science Foundation of China (No. 41572078, 41872106), BGEG and GPMR laboratory funds (GKZ18Y660, GPMR201609), and the Fundamental Research Funds for the Central Universities (CUG160604) granted to JY, and Australian Research Council grant FL160100168 to PAC.

Appendix A. Supplementary material

Supplementary material related to this article can be found online at https://doi.org/10.1016/j.epsl.2020.116074.

References

Cawood, P.A., Wang, Y., Xu, Y., Zhao, G., 2013. Locating South China in Rodinia and Gondwana: a fragment of greater India lithosphere? Geology 41, 903–906.
Chen, B., Joachimski, M.M., Wang, X.-d., Shen, S.-z., Qi, Y.-p., Qie, W.-k., 2016. Ice volume and paleoclimate history of the Late Paleozoic Ice Age from conodont apatite oxygen isotopes from Naqing (Guizhou China). Palaeogeogr. Palaeoclimatol. Palaeoecol. 448, 151–161.
Chen, J., Montañez, I.P., Qi, Y., Shen, S., Wang, X., 2018. Strontium and carbon isotopic evidence for decoupling of pCO_2 from continental weathering at the apex of the late Paleozoic glaciation. Geology 46 (5), 395–398.
Condon, D.J., Schoene, B., McLean, N.M., Bowring, S.A., Parrish, R.R., 2015. Metrology and traceability of U-Pb isotope dilution geochronology (EARTHTIME Tracer Calibration Part I). Geochim. Cosmochim. Acta 164, 464–480.
Corfu, F., Dahlgren, S., 2008. Perovskite U-Pb ages and the Pb isotopic composition of alkaline volcanism initiating the Permo-Carboniferous Oslo Rift. Earth Planet. Sci. Lett. 265, 256–269.
Davydov, V.I., Biakov, A.S., 2015. Discovery of shallow-marine biofacies conodonts in a bioherm within the Carboniferous-Permian transition in the Omolon Massif, NE Russia near the North Paleo-pole: correlation with a warming spike in the southern hemisphere. Gondwana Res. 28, 888–897.
Davydov, V.I., Haig, D.W., McCartain, E., 2013. A latest Carboniferous warming spike recorded by a fusulinid-rich bioherm in Timor Leste: implications for East Gondwana deglaciation. Palaeogeogr. Palaeoclimatol. Palaeoecol. 376, 22–38.
Dessert, C., Dupré, B., François, L.M., Schott, J., Gaillardet, J., Chakrapani, G., Bajpai, S., 2001. Erosion of Deccan Traps determined by river geochemistry: impact on the global climate and the $^{87}Sr/^{86}Sr$ ratio of seawater. Earth Planet. Sci. Lett. 188, 459–474.
Dinis, P., Garzanti, E., Vermeesch, P., Huvi, J., 2017. Climatic zonation and weathering control on sediment composition (Angola). Chem. Geol. 467, 110–121.
Ernst, R.E., Youbi, N., 2017. How Large Igneous Provinces affect global climate, sometimes cause mass extinctions, and represent natural markers in the geological record. Palaeogeogr. Palaeoclimatol. Palaeoecol. 478, 30–52.
Eros, J.M., Montañez, I.P., Osleger, D.A., Davydov, V.I., Nemyrovska, T.I., Poletaev, V.I., Zhykalyak, M.V., 2012. Sequence stratigraphy and onlap history of the Donets Basin, Ukraine: insight into Carboniferous icehouse dynamics. Palaeogeogr. Palaeoclimatol. Palaeoecol. 313–314, 1–25.
Fedo, C.M., Nesbitt, H.W., Young, G.M., 1995. Unraveling the effects of potassium metasomatism in sedimentary rocks and paleosols, with implications for paleoweathering conditions and provenance. Geology 23, 921–924.
Feng, B., 2012. Study on coal-accumulating characteristic of Shanxi Formation and low Shihezi Formation in Yongcheng coal filed, Henan Province. J. Henan Polytech. Univ. 31, 177–181 (in Chinese with English abstract).
Ferrier, K.L., Riebe, C.S., Hahm, W.J., 2016. Testing for supply-limited and kinetic-limited chemical erosion in field measurements of regolith production and chemical depletion. Geochem. Geophys. Geosyst. 17, 2270–2285.
Fielding, C.R., Frank, T.D., Birgenheiner, L.P., Rygel, M.C., Jones, A.J., Roberts, J., 2008. Stratigraphic imprint of the Late Paleozoic Ice Age in eastern Australia: a record of alternating glacial and nonglacial climate regime. J. Geol. Soc. (Lond.) 165, 129–140.
Gao, F., Ding, H., Wan, X., 2005. Taxonomic revision of conodont Sweetognathus species in the uppermost Taiyuan Formation, Yuhuai Basin and its significance. Acta Micropalaeontol. Sin. 22 (4), 370–382.
Gao, S., Luo, T., Zhang, B., Zhang, H., Han, Y., Zhao, Z., Hu, Y., 1998. Chemical composition of the continental crust as revealed by studies in East China. Geochim. Cosmochim. Acta 62, 1959–1975.
Garzanti, E., Resentini, A., 2016. Provenance control on chemical indices of weathering (Taiwan river sands). Sediment. Geol. 236, 81–95.
Garzanti, E., Angiolini, L., Brunton, H., Sciunnach, D., Balini, M., 1998. The Bashkirian "Fenestella Shales" and the Moscovian "Chaetetid Shales" of the Tethys Himalaya (South Tibet, Nepal and India). J. Asian Earth Sci. 16, 119–141.
Garzanti, E., Padoan, M., Peruta, L., Setti, M., Najman, Y., Villa, I.M., 2013. Weathering geochemistry and Sr-Nd fingerprints of equatorial upper Nile and Congo muds. Geochem. Geophys. Geosyst. 14, 292–316.
Griffis, N.P., Montañez, I.P., Mundil, R., Richey, J., Isbell, J., Fedorchuk, N., Linol, B., Iannuzzi, R., Vesely, F., Mottin, T., da Rosa, E., Keller, B., Yin, Q.-Z., 2019. Coupled stratigraphic and U-Pb zircon age constraints on the late Paleozoic icehouse-to-greenhouse turnover in south-central Gondwana. Geology 47 (12), 1146–1150.
Griffis, N.P., Mundil, R., Montañez, I.P., Isbell, J., Fedorchuk, N., Vesely, F., Iannuzzi, R., Yin, Q.-Z., 2018. A new stratigraphic framework built on U-Pb single-zircon TIMS ages and implications for the timing of the penultimate icehouse (Paraná Basin, Brazil). Geol. Soc. Am. Bull. 130, 848–858.
Hamilton, M.A., Pearson, D.G., 2011. Precise U-Pb age for the Great Whin Dolerite Complex, N.E. England and its significance. In: Srivastava, R.K. (Ed.), Dyke Swarms: Keys for Geodynamic Interpretation. Springer, Berlin, pp. 495–507.
Haq, B.U., Schutter, S.R., 2008. A chronology of Paleozoic sea-level changes. Science 322, 64–68.
Heeremans, M., Timmerman, M.J., Kirstein, L.A., Faleide, J.I., 2004. New constraints on the timing of late Carboniferous-early Permian volcanism in the central North Sea. In: Wilson, M., Neumann, E.R., Davies, G.R., Timmerman, M.J., Heeremans, M., Larsenet, B.T. (Eds.), Permo-Carboniferous Magmatism and Rifting in Europe. In: Geol. Soc. (Lond.) Spec. Publ., vol. 223, pp. 177–194.
Henderson, C.M., 2018. Permian conodont biostratigraphy. In: Lucas, S.G., Shen, S.Z. (Eds.), The Permian Timescale. In: Geol. Soc. (Lond.) Spec. Publ., vol. 450, pp. 119–142.
Henderson, C.M., Wardlaw, B.R., Davydov, V.I., Schmitz, M.D., Schiappa, T.A., Tierney, K.E., Shen, S., 2012. Proposal for base-Kungurian GSSP. Permophiles 56, 8–21.
Isbell, J.L., Henry, L.C., Gulbranson, E., Limarino, C.O., Fraiser, M.L., Koch, Z.J., Ciccioli, P.L., Dineen, A.A., 2012. Glacial paradoxes during the late Paleozoic ice age: evaluating the equilibrium line altitude as a control on glaciation. Gondwana Res. 22, 1–19.
Jones, M.T., Jerram, D.A., Svensen, H.H., Grove, C., 2016. The effects of large igneous provinces on the global carbon and sulphur cycles. Palaeogeogr. Palaeoclimatol. Palaeoecol. 441, 4–21.
Kasbohm, J., Schoene, B., 2018. Rapid eruption of the Columbia River flood basalt and correlation with the mid-Miocene climate optimum. Sci. Adv. 4, eaat8223.
Korte, C., Ullmann, C.V., 2018. Permian strontium isotope stratigraphy. In: Lucas, S.G., Shen, S.Z. (Eds.), The Permian Timescale. In: Geol. Soc. (Lond.) Spec. Publ., vol. 450, pp. 105–118.
Johnsson, M.J., 1993. The system controlling the composition of clastic sediments. In: Johnsson, M.J., Basu, A. (Eds.), Processes Controlling the Composition of Clastic Sediments. In: Spec. Pap. Geol. Soc. Am., vol. 284, pp. 1–19.
Lupker, M., France-Lanord, C., Galy, V., Lavé, J., 2013. Increasing chemical weathering in the Himalayan system since the Last Glacial Maximum. Earth Planet. Sci. Lett. 365, 243–252.
McKay, D.I.A., Tyrrell, T., Wilson, P.A., Foster, G.L., 2014. Estimating the impact of the cryptic degassing of Large Igneous Province: a mid-Miocene case-study. Earth Planet. Sci. Lett. 403, 254–262.

Neumann, E.R., Wilson, M., Heeremans, M., Spencer, E.A., Obst, K., Timmerman, M.J., Kirstein, L., 2004. Carboniferous-Permian rifting and magmatism in southern Scandinavia, the North Sea and northern Germany: a review. In: Wilson, M., Neumann, E.R., Davies, G.R., Timmerman, M.J., Heeremans, M., Larsenet, B.T. (Eds.), Permo-Carboniferous Magmatism and Rifting in Europe. In: Geol. Soc. (Lond.) Spec. Publ., vol. 223, pp. 11–40.

Monaghan, A.A., Pringle, M.S., 2004. $^{40}Ar/^{39}Ar$ geochronology of Carboniferous-Permian volcanism in the Midland Valley, Scotland. In: Wilson, M., Neumann, E.R., Davies, G.R., Timmerman, M.J., Heeremans, M., Larsenet, B.T. (Eds.), Permo-Carboniferous Magmatism and Rifting in Europe. In: Geol. Soc. (Lond.) Spec. Publ., vol. 223, pp. 219–241.

Montañez, I.P., Poulsen, C.J., 2013. The late Paleozoic Ice Age: an evolving paradigm. Annu. Rev. Earth Planet. Sci. 41, 629–656.

Montañez, I.P., McElwain, J.C., Poulsen, C.J., White, J.D., DiMichele, W.A., Wilson, J.P., Griggs, G., Hren, M.T., 2016. Climate, pCO_2 and terrestrial carbon cycle linkages during late Paleozoic glacial-interglacial cycles. Nat. Geosci. 9, 824–828.

Nesbitt, H.W., Young, G.M., 1982. Early Proterozoic climates and plate motions inferred from major element chemistry of lutites. Nature 299, 715–717.

Parker, A., 1970. An index of weathering for silicate rocks. Geol. Mag. 107, 501–504.

Pei, F., 2004. The North China type Permo-Carboniferous fusulinid and conodont biostratigraphic units of Henan Province. J. Stratigr. 28, 344–353 (in Chinese with English abstract).

Phillips, T.B., Magee, C., Jackson, C.A.L., Bell, R.W., 2018. Determining the three-dimensional geometry of a dike swarm and its impact on later rift geometry using seismic reflection data. Geology 46, 119–122.

Rasmussen, C., Brantley, S., Richter, D. deB, Blum, A., Dixon, J., White, A.F., 2011. Strong climate and tectonic control on plagioclase weathering in granitic terrain. Earth Planet. Sci. Lett. 301, 521–530.

Riebe, C.S., Kirchner, J.W., Finkel, R.C., 2004. Erosional and climatic effects on long-term chemical weathering rates in granitic landscapes spanning diverse climate regimes. Earth Planet. Sci. Lett. 224, 547–562.

Self, S., Widdowson, M., Thordarson, T., Jay, A.E., 2006. Volatile fluxes during flood basalt eruptions and potential effects on the global environment: a Deccan perspective. Earth Planet. Sci. Lett. 248, 518–532.

Schaller, M.F., Wright, J.D., Kent, D.V., Olsen, P.E., 2012. Rapid emplacement of the Central Atlantic Magmatic Province as a net sink for CO_2. Earth Planet. Sci. Lett. 323–324, 27–39.

Scheffler, K., Buehmann, D., Schwark, L., 2006. Analysis of late Palaeozoic glacial to postglacial sedimentary successions in South Africa by geochemical proxies – response to climate evolution and sedimentary environment. Palaeogeogr. Palaeoclimatol. Palaeoecol. 240, 184–203.

Scheffler, K., Hoernes, S., Schwark, L., 2003. Global changes during Carboniferous-Permian glaciation of Gondwana: linking polar and equatorial climate evolution by geochemical proxies. Geology 31, 605–608.

Schmitz, M.D., Davydov, V.I., 2012. Quantitative radiometric and biostratigraphic calibration of the Pennsylvanian-Early Permian (Cisuralian) time scale and pan-Euramerican chronostratigraphic correlation. Geol. Soc. Am. Bull. 124, 549–577.

Shen, S., Zhang, H., Zhang, Y., Yuan, D., Chen, B., He, W., Mu, L., Wang, W., Chen, J., Wu, Q., Cao, C., Wang, Y., Wang, X., 2019. Permian integrative stratigraphy and timescale of China. Sci. China Earth Sci. 62 (1), 154–188.

Soreghan, G.S., Soreghan, M.J., Heavens, N.G., 2019. Explosive volcanism as a key driver of the late Paleozoic ice age. Geology 47, 600–604.

Stollhofen, H., Werner, M., Stanistreet, I.G., Armstrong, R.A., 2008. Single-zircon U-Pb dating of Carboniferous-Permian tuffs, Namibia, and the intercontinental deglaciation cycle framework. In: Fielding, C.R., Frank, T.D., Isbell, J.L. (Eds.), Resolving the Late Paleozoic Ice Age in Time and Space. In: Spec. Pap. Geol. Soc. Am., vol. 441, pp. 83–96.

Taboada, A.C., Neves, J.P., Weinschütz, L.C., Pagani, M.A., Simões, M.G., 2016. Eurydesma–Lyonia fauna (Early Permian) from the Itararé group, Paraná Basin (Brazil): a paleobiogeographic W–E trans-Gondwanan marine connection. Palaeogeogr. Palaeoclimatol. Palaeoecol. 449, 431–454.

Tabor, N.J., DiMichele, W.A., Montañez, I.P., Chaney, D.S., 2013. Late Paleozoic continental warming of a cold tropical basin and floristic change in western Pangea. Int. J. Coal Geol. 119, 177–186.

Tabor, N.J., Poulsen, C.J., 2008. Palaeoclimate across the Late Pennsylvanian-Early Permian tropical palaeolatitudes: a review of climate indicators, their distribution and relation to palaeophysiographic climate factors. Palaeogeogr. Palaeoclimatol. Palaeoecol. 268, 293–310.

Timmerman, M.J.M., Heeremans, M., Kirstein, L.A., Larsen, B.T., Spencer-Dunworth, E.A., Sundvoll, B., 2009. Linking changes in tectonic style with magmatism in northern Europe during the late Carboniferous to latest Permian. Tectonophysics 473, 375–390.

Torsvik, T.H., van der Voo, R., Doubrovine, P.V., Burke, K., Steinberger, B., Ashwal, L.D., Trønnes, R.G., Webb, S.J., Bull, A.L., 2014. Deep mantle structure as a reference frame for movements in and on the Earth. Proc. Natl. Acad. Sci. USA 17, 8735–8740.

Torsvik, T.H., Smethurst, M.A., Burke, K., Steinberger, B., 2008. Long term stability in deep mantle structure: evidence from the ~300 Ma Skagerrak-Centered Large Igneous Province (the SCLIP). Earth Planet. Sci. Lett. 267, 444–452.

von Eynatten, H., Tolosana-Delgado, R., Karuius, V., Bachmann, K., Caracciolo, L., 2016. Sediment generation in humid Mediterranean setting: grain-size and source-rock control on sediment geochemistry and mineralogy (Sila Massif, Calabria). Sediment. Geol. 336, 68–80.

Wang, H., 1985. Atlas of the Palaeogeography of China. Cartographic Publishing House, Beijing, China. 143 pp.

Wang, H., Qi, Y., 2003. Review of Carboniferous-Permian conodont biostratigraphy in North China. Acta Micropalaeontol. Sin. 9, 228–230 (in Chinese with English abstract).

Yang, J., Cawood, P.A., Du, Y., Feng, B., Yan, J., 2014. Global continental weathering trends across the Early Permian glacial to postglacial transition: correlating high- and low- paleolatitude sedimentary records. Geology 42, 835–838.

Yang, J., Cawood, P.A., Du, Y., Li, W., Yan, J., 2016. Reconstructing Early Permian tropical climates from chemical weathering indices. Geol. Soc. Am. Bull. 128, 739–751.

Yang, J., Yan, J., Huang, Y., 2017. The Earth's penultimate icehouse-to-greenhouse climate transition and related sedimentary records in low-latitude regions of eastern Tethys. Acta Sediment. Sin. 35 (5), 981–993 (in Chinese with English abstract).